



Effect of partial substitution of Ta₂O₅ by ZrO₂ on the structure and ionic conductivity of Li₂O-Ta₂O₅-2 SiO₂ glass and glass-ceramics

Qian Zhang^{1,2,*}, Ziwei Li¹, Ruixiong Liao¹, Haizhong Wang¹, Boyuan Wang¹, Longxin Xie¹, Shan Wu^{1,*}, Dmytro Sydorov¹

¹Metallurgical Division of Materials Chemistry, Key Laboratory of Battery Power and Materials Jiangxi Province, Jiangxi University of Science and Technology, Ganzhou, 341000, China

²Yichun Lithium Battery New Energy Industry Research Institute of Jiangxi University of Science and Technology, Yichun, 336000, China

Received 1 November 2023; Received in revised form 26 January 2024; Accepted 20 February 2024

Abstract

LiTaSiO₅ system is considered as type of solid electrolyte with great potential for application as ionic conductor. It is well-known that it is difficult to obtain pure dense LiTaSiO₅ phase by traditional synthesis methods, because dielectric LiTaO₃ phase easily precipitates during synthesis, which affects ionic conductivity. In this work, a glass-ceramic electrolyte with main LiTaSiO₅ phase was obtained by controlled crystallization of Li₂O-Ta₂O₅-2 SiO₂ glass without porosity. The precipitation of LiTaO₃ phase at the grain boundary was effectively inhibited by adding an appropriate amount of ZrO₂. Among all the glass-ceramic samples, the glass containing 4.76 mol% ZrO₂ had the maximum ionic conductivity of 8.40×10^{-6} S/cm at 25 °C, which is two order of magnitude greater than the ionic conductivity of the matrix glass. These glass-ceramic samples have the potential to be used as solid electrolytes in electrochemical applications.

Keywords: glass ceramics, silicate, ionic conductivity, IR spectroscopy, impedance

I. Introduction

Electrochemical energy storage has been widely utilized, with lithium-ion batteries (LIBs) being a highly recognized technology due to their high energy density, high operating voltage, long cycle life and environmental friendliness [1,2]. However, traditional commercial lithium-ion batteries have safety hazards such as combustion and explosion due to the use of organic liquid electrolytes [3]. Therefore, it makes sense to find suitable materials to replace the organic liquid electrolyte [4,5]. Inorganic solid electrolytes discovered in recent years, such as Li₁₀GeP₂S₁₂ (LGPS) [6], Li₇P₃S₁₁ [7], garnet Li₇La₃Zr₂O₁₂ (LLZO) [8–10], NASICON [11] and Li_{1.3}Al_{0.3}Ti_{1.7}(PO₄)₃ (LATP) [12], can replace organic liquid electrolyte materials with appropriate stability of lithium, wide electrochemical window and high energy density.

In particular, LiTaSiO₅ (LTSO) stands out as a recently discovered lithium-ion electrolyte material. Existing research on the LTSO was predominantly focused on traditional ceramic processing even though the sintering process often leads to the formation of pores. In contrast, glass materials offer higher density compared to ceramics. As observed by Tan *et al.* [13], it is possible to synthesize pure-phase glass-ceramic electrolytes by carefully controlling the crystallization process within Li₂O-Ta₂O₅-SiO₂ ternary glass system. The precipitation of a crystalline phase with high conductivity holds the potential to enhance the overall ionic conductivity of the glass electrolyte [14,15]. This method proves effective in improving both density and conductivity of the glass material. However, previous investigations [16–18] indicated that sintered LTSO materials can contain a substantial fraction of the precipitated LTO phase, a factor that constrains further improvements in LTSO conductivity.

The introduction of dopants in glass-ceramic materials has been demonstrated as a reliable approach to

* Corresponding author: tel: +86 13970784755
e-mail: zhangqian@jxust.edu.cn (Q. Zhang)
9120160038@jxust.edu.cn (S. Wu)

avoid phase precipitation [19,20]. Furthermore, previous investigations have validated the capacity of appropriate Zr^{4+} doping to augment room temperature ionic conductivity and stability within LTSO [16,18]. Building upon these insights, we aimed to introduce Zr^{4+} ions into LTSO and generate glass-ceramics with a pure-phase structure, encompassing the composition $(1+x)/2Li_2O-(1-x)/2Ta_2O_5-xZrO_2-SiO_2$, ultimately yielding dense materials. Herein, precursor glasses with different ZrO_2 contents were prepared by melting-quenching method and the corresponding glass-ceramics were prepared by single-step heat treatment. The effects of different Zr^{4+} doping amounts on the crystal structure and electrical properties of $Li_{1+x}Ta_{1-x}Zr_xSiO_5$ electrolytes were studied.

II. Experimental

2.1. Glass and glass-ceramics synthesis

$(1+x)/2Li_2O-(1-x)/2Ta_2O_5-xZrO_2-SiO_2$ parent glasses, where molar ratio x was 0, 0.05, 0.10, 0.15 and 0.20, were produced by the melt quenching method. The used raw materials, Li_2CO_3 (99.5%, AR), Ta_2O_5 (99.5%, AR), ZrO_2 (99.5%, AR) and SiO_2 (99.5%, AR), were mixed in the stoichiometric amounts and an excess of 10% Li_2CO_3 was added to compensate for the loss of lithium due to volatilization during heating. The chemical compositions of each parent glass are shown in Table 1. The raw materials were weighed accurately and mixed in agate mortar before being transferred to a zirconia crucible. The obtained mixtures were then preheated at 450 °C for 2 h to decompose the raw materials and remove CO_2 and H_2O . Then the temperature was increased to 1620 °C at a rate of 5 °C/min and held for 1 h. The resulting melts were quickly pressed and shaped with preheated steel plates, and annealed at 550 °C for 3 h. Subsequently, glassy flakes with a thickness of approximately 1.5 mm were obtained and cut into rectangular blocks of 10 × 10 mm. Finally, the samples were polished and the corresponding glass-ceramics were prepared by heat treatment at 980 °C for 10 h.

2.2. Glass and glass-ceramics characterization

X-ray diffraction (XRD) patterns were recorded at room temperature on the MiniFlex600 X-ray diffractometer using a $Cu-K\alpha_1$ radiation, with operating voltage of 40 kV and operating current of 15 mA. The data were collected at room temperature with a step size of 0.02° and scan angle range of 10–80°. Infrared spec-

tra were recorded using an FTIR-1500 Fourier transform infrared spectrometer in transmission mode, with measurements conducted over an energy range of 1300–400 cm^{-1} . The density of both glass and glass-ceramic samples was determined using the Archimedes' method, with the average of 8–10 measurements being reported. The molar volume (V_m) was calculated through the equation:

$$V_m = \frac{1}{\rho} \sum X_i \cdot M_i \quad (1)$$

where X_i is the molar fraction and M_i is the total molecular weight of the i^{th} component. The glass transition temperature and crystallization peak temperature were determined via differential scanning calorimetry (DSC) using a Netzsch STA449C differential scanning calorimeter, with measurements conducted in air at a heating rate of 10 °C/min. The experimental error associated with glass transition temperature and crystallization temperature was ± 3 °C. The samples were subjected to HF etching for 10 s, and SEM images were acquired using a Zeiss Crossbeam 340 scanning electron microscope analyser. The AC impedance of the glass samples was measured using an Agilent 4294A impedance analyser with a frequency range of 40 to 110×10^6 Hz and an amplitude of 50 mV, while the impedance of the glass-ceramic samples was determined using an Autolab ChemStation in the frequency range of 1 to 1×10^6 Hz and at temperatures ranging from 25–150 °C. The conductivity and activation energy of the sample can be calculated from the fitting results and the following two formulas:

$$\sigma = \frac{L}{R \cdot S} \quad (2)$$

$$\sigma \cdot T = A \cdot \exp\left(-\frac{E_a}{k \cdot T}\right) \quad (3)$$

where σ is the ion conductivity, L is the sample thickness, R is the impedance value of the fitted equivalent circuit, S is the measurement surface area of the sample, E_a is the activation energy of the sample, and A , k and T are the pre-exponential factor, the Boltzmann's constant and absolute temperature, respectively.

III. Results and discussion

3.1. Structure of precursor glasses

The XRD diffraction spectra of the precursor glasses are shown in Fig. 1. The characteristic XRD peaks of all samples are very broad, indicating that the resulting

Table 1. Chemical composition of glasses

Sample	Li ₂ O [mol%]	Ta ₂ O ₅ [mol%]	ZrO ₂ [mol%]	SiO ₂ [mol%]
basic glass	25	25	0	50
glass with 0.05 ZrO ₂	25.61	23.17	2.44	48.78
glass with 0.10ZrO ₂	26.19	21.43	4.76	47.62
glass with 0.15ZrO ₂	26.74	19.77	6.98	46.51
glass with 0.20ZrO ₂	27.27	18.18	9.09	45.45

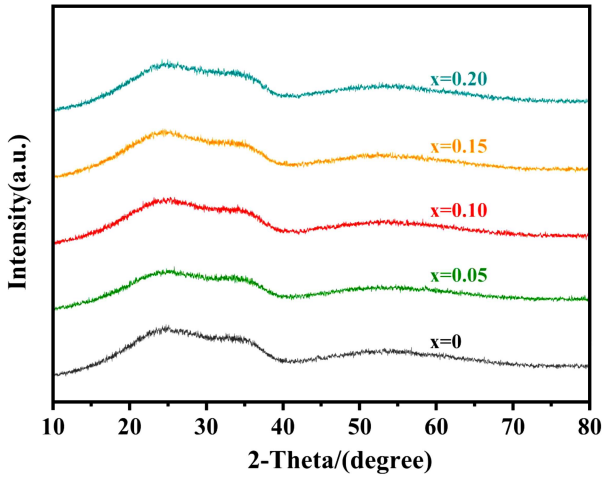


Figure 1. XRD patterns of $(1+x)/2\text{Li}_2\text{O}-(1-x)/2\text{Ta}_2\text{O}_5-x\text{ZrO}_2-\text{SiO}_2$ precursor glass samples

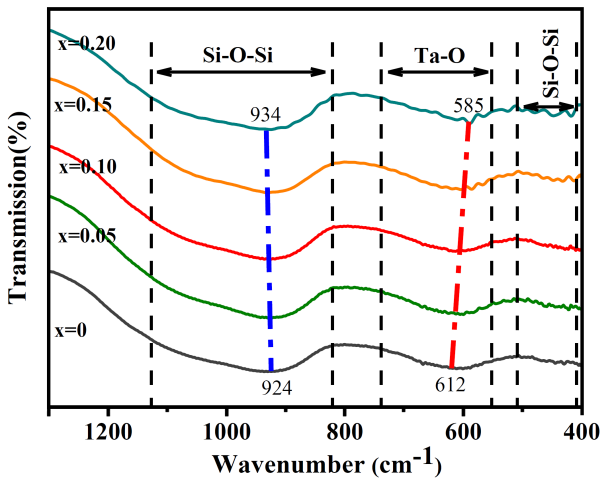


Figure 2. FTIR spectra of $(1+x)/2\text{Li}_2\text{O}-(1-x)/2\text{Ta}_2\text{O}_5-x\text{ZrO}_2-\text{SiO}_2$ precursor glass samples

samples are amorphous glasses.

Figure 2 illustrates the infrared (IR) absorption spectra of all precursor glasses in wavenumber region of $1200\text{--}400\text{ cm}^{-1}$. The infrared absorption spectra of the precursor glass samples revealed significant absorption bands in the ranges of $509\text{--}412\text{ cm}^{-1}$, $739\text{--}552\text{ cm}^{-1}$ and $1127\text{--}821\text{ cm}^{-1}$. Specifically, the absorption peaks at $447\text{--}409\text{ cm}^{-1}$ are attributed to the bending and symmetric vibrations of the Si–O–Si bond in SiO_4 unit [21,22], while the peak at $612\text{--}585\text{ cm}^{-1}$ is associated with mixed Ta–O or Si–O–Ta bond bending vibrations [23]. Within the range of $1127\text{--}821\text{ cm}^{-1}$, two asymmetric Si–O–Si stretching vibrations are observed, one around 1000 cm^{-1} and the other within the range of $1127\text{--}821\text{ cm}^{-1}$. The substitution of some Ta_2O_5 by ZrO_2 resulted in redshift of the peak at $612\text{--}585\text{ cm}^{-1}$ and slight decrease of its intensity. In contrast, the peak at $934\text{--}924\text{ cm}^{-1}$ shifts to higher wavenumber (blueshift) with a slight increase in its intensity. The transition metal ion Ta^{5+} exists in the glass network as an intermediate, which increases the bridge oxygen

number and makes the network more compact [24]. The Si–O–Si bonds break with the insertion of $[\text{TaO}_6]$ units, leading to the depolymerization of the silicon-oxygen skeleton in the glass network, disrupting the network structure and forming clusters of TaO_6 in the glass [25]. In addition, the high field strength and coordination number of Ta^{5+} attract surrounding free oxygen ions or connect to silicon through bridging oxygen, increasing the amount of non-bridging oxygen in the glass network. This phenomenon has been reported in other studies related to transition metal materials [24,26]. The field strength and coordination number of Zr^{4+} are weaker than those of Ta^{5+} , which also increases the amount of bridging oxygen in the glass network. Therefore, Zr^{4+} contributes more to the weakening of the glass network than Ta^{5+} . The absorption peak at $612\text{--}585\text{ cm}^{-1}$ was redshifted and the absorption peak intensity decreased slightly due to the reduction in the amount of non-bridging oxygen and an increase in the amount of bridging oxygen brought about by the decrease in Ta^{5+} . On the other hand, Zr^{4+} combines with silicon atoms to form Si–O–Zr bonds with high vibration frequency and the characteristic absorption peak frequency is generally observed at $\sim 1030\text{ cm}^{-1}$ [27]. This results in a peak-absorbing blueshift at $934\text{--}924\text{ cm}^{-1}$ with a slight increase in intensity.

The density roughly reflects the composition and underlying structure of the glass. The molar volume indicates the degree of filling of the structural glass units, which is determined by the volume of the glass network structural units and the degree of mesh filling. The density and molar volume of the precursor glasses with different ZrO_2 content are presented in Fig. 3. These data illustrate that as the ZrO_2 content increases, the density of the glass decreases from 4.98 to 4.66 g/cm^3 and the molar volume drops from 29.25 to $26.91\text{ cm}^3/\text{mol}$.

Both Ta^{5+} and Zr^{4+} are high-field strength transition metal ions with high coordination number. The $[\text{TaO}_6]$ cluster inside the glass will destroy the internal network structure of the glass and make the structure sparse. Due to the longer Ta–O bonds compared to Zr–O bonds,

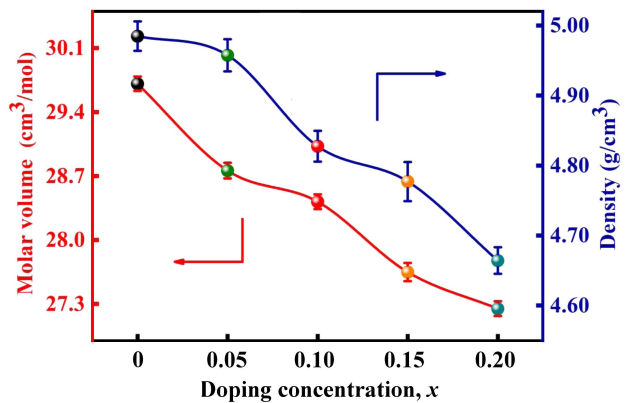


Figure 3. Trends of density and molar volume of $(1+x)/2\text{Li}_2\text{O}-(1-x)/2\text{Ta}_2\text{O}_5-x\text{ZrO}_2-\text{SiO}_2$ precursor glass samples

the volume of the glass network structure increases. As shown in Fig. 3, the density and molar volume of the precursor glasses follow the same trend. FTIR spectral analysis indicates that the relative atomic mass of Ta is much larger than those of Zr and Li in the glass network system after partial substitution of Ta_2O_5 by ZrO_2 . The increase of the relative atomic masses of Zr and Li is not sufficient to compensate for the loss, resulting in a decrease in density. Moreover, the partial substitution of Ta^{5+} by Zr^{4+} in the structure reduces the proportion of Ta–O bonds in the system, which plays a dominant role in the denseness of the network structure. In addition, Zr^{4+} forms Si–O–Zr bonds with silicon-oxygen bonds as intermediates connecting glass networks, increasing the density of glass. The combined effect of these two aspects leads to an increase in the density of the $(1+x)/2\text{Li}_2\text{O}-(1-x)/2\text{Ta}_2\text{O}_5-x\text{ZrO}_2\text{-SiO}_2$ precursor glass and a decrease in molar volume.

The differential scanning calorimetry (DSC) curves of precursor glasses doped with different amounts of ZrO_2 with a temperature ramp rate of $10^\circ\text{C}/\text{min}$ are shown in Fig. 4. T_g , T_x and T_c represent glass transition temperature, onset of crystallization temperature and crystallization temperature, respectively. The thermal stability of the formed glass against crystallization was evaluated according to the calculation of the thermal parameter ΔT given by Dietzel and Saad-Paulin:

$$\Delta T = T_x - T_g \quad (4)$$

ΔT reflects the anti-crystallization ability of glass melt and its ability to maintain its amorphous state dur-

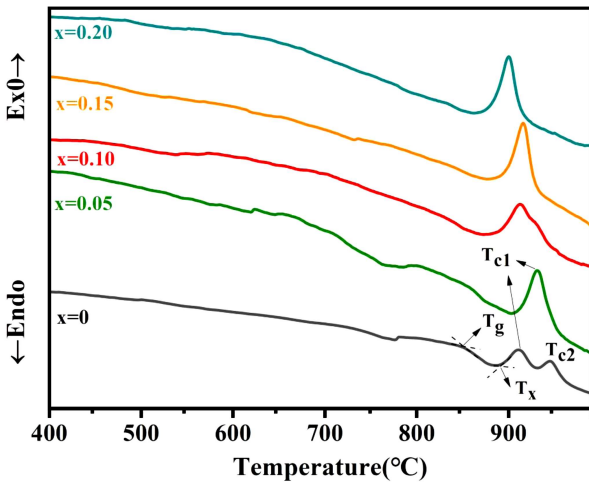


Figure 4. DSC curves of $(1+x)/2\text{Li}_2\text{O}-(1-x)/2\text{Ta}_2\text{O}_5-x\text{ZrO}_2\text{-SiO}_2$ precursor glasses

ing cooling and solidification process [28,29]. The numerical values for each characteristic temperature and ΔT are presented in Table 2. The undoped precursor glass has two crystallization temperatures, T_{c1} and T_{c2} . The addition of ZrO_2 resulted in an increase in the calculated value of ΔT . These observations, combined with the results of FTIR, density and molar volume studies, suggest that Ta^{5+} acts as an inhomogeneous nucleating agent inside the glass network, generating a large number of inhomogeneous nucleation sites and inducing phase separation in the glass due to its high field strength. Ta^{5+} as an intermediate also facilitates cross-linking between covalent bonds, resulting in tighter network connection and higher glass transition temperatures. As Ta^{5+} is gradually replaced by Zr^{4+} , the bond strength and coordination number decrease, and Zr^{4+} has a smaller contribution to network connectivity than Ta^{5+} , leading to a reduction in the glass transition temperature. Zr^{4+} forms ZrO_n clusters after doping, which produces many non-bridging oxygen ions through the precipitation of nucleating agents, which promotes the ability of glass formation [30]. Thus, the addition of ZrO_2 suppresses the phase decomposition in the $(1+x)/2\text{Li}_2\text{O}-(1-x)/2\text{Ta}_2\text{O}_5-x\text{ZrO}_2\text{-SiO}_2$ precursor glasses and significantly reduces the crystallization temperature of the glasses. These findings provide valuable insights for future studies on glass crystallization.

3.2. Structure of glass-ceramics

The DSC curves of the precursor glasses with different ZrO_2 content indicate that the glass transition temperature and the crystallization peak temperature are in the range of $426\text{--}766^\circ\text{C}$ and $900\text{--}945^\circ\text{C}$, respectively. After numerous attempts, $\text{Li}_{1+x}\text{Ta}_{1-x}\text{Zr}_x\text{SiO}_5$ glass-ceramic electrolytes were successfully fabricated by using single-stage heat treatment (SSHT) at 980°C for 10 h. X-ray diffraction analyses were conducted on all glass ceramics (Fig. 5a) and confirmed the presence of LiTaSiO_5 phase. Based on the observations in Fig. 5b, it is evident that the primary X-ray diffraction peak of LTSO phase undergoes a shift towards lower angles upon ZrO_2 addition. This shift indicates the successful substitution of Ta^{5+} ions (ionic radius of 0.64 \AA) with Zr^{4+} ions (ionic radius of 0.72 \AA) within the lattice, leading to an increase in lattice spacing [31,32]. At a doping concentration of $x = 0.1$, the primary X-ray diffraction peak of LTSO phase reaches its maximum intensity and becomes sharper, indicating the highest level of crystallinity at this concentration [33]. Excessive doping, however, introduces lattice distortion, in-

Table 2. Characteristic temperature and stability parameters of the precursor glasses (ΔT)

Sample	T_g [$\pm 3^\circ\text{C}$]	T_x [$\pm 3^\circ\text{C}$]	T_{c1} [$\pm 3^\circ\text{C}$]	T_{c2} [$\pm 3^\circ\text{C}$]	ΔT [$\pm 3^\circ\text{C}$]
basic glass	852	884	910	945	32
glass with 0.05 ZrO_2	859	911	930		52
glass with 0.10 ZrO_2	831	885	912		54
glass with 0.15 ZrO_2	837	895	915		58
glass with 0.20 ZrO_2	833	880	900		47

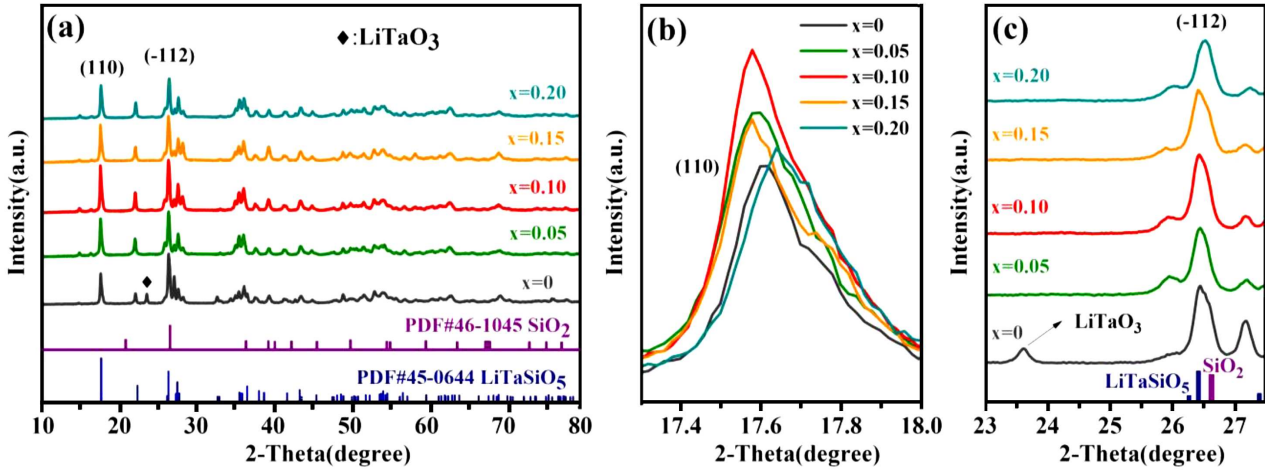


Figure 5. XRD patterns of $\text{Li}_{1+x}\text{Ta}_{1-x}\text{Zr}_x\text{SiO}_5$ glass-ceramics (a) and corresponding enlarge regions (b,c)

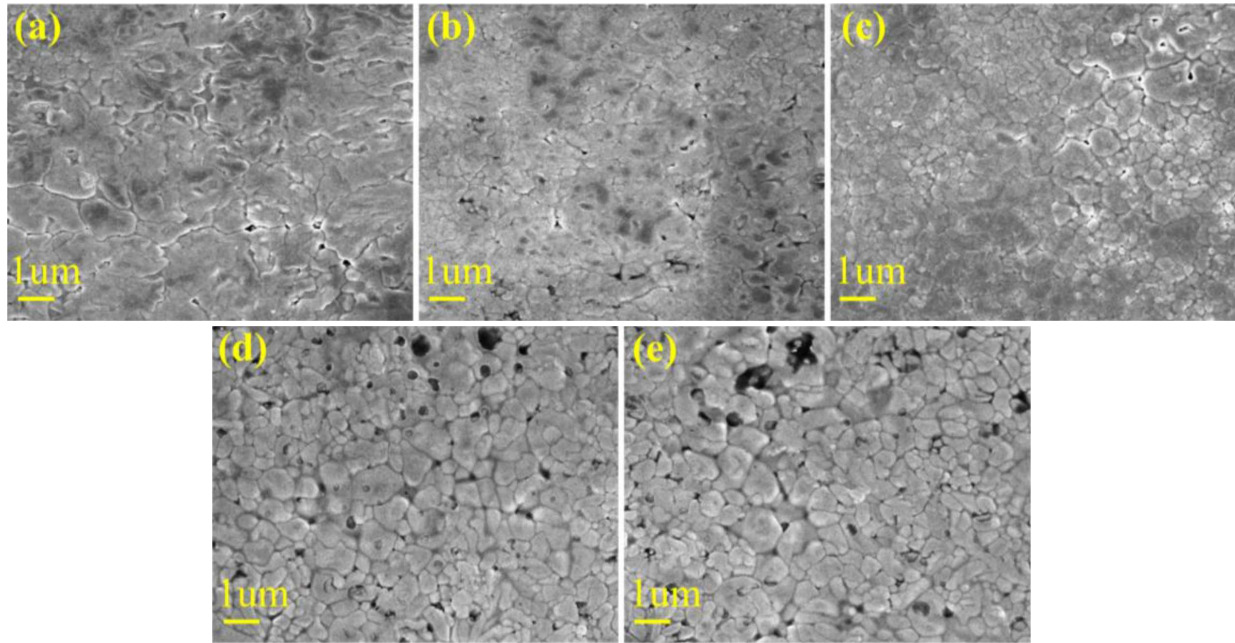


Figure 6. SEM micrographs of $\text{Li}_{1+x}\text{Ta}_{1-x}\text{Zr}_x\text{SiO}_5$ glass-ceramic surface: a) $x = 0$, b) $x = 0.05$, c) $x = 0.1$, d) $x = 0.15$ and e) $x = 0.2$

creasing the probability of structural collapse. Consequently, the diffraction peak of the (110) crystal plane shifts to higher angles when $x = 0.2$. Furthermore, the partial replacement of Ta^{5+} by Zr^{4+} significantly impacts the crystalline phase composition of the microcrystalline glass electrolyte. When $x = 0$, the strongest X-ray diffraction peak of LTSO phase is noticeably weaker than the diffraction peak at approximately 26.5° on the left side. As shown in Fig. 5c, this is the result of the superposition of the $(\bar{1}12)$ crystal plane diffraction peak and the SiO_2 main peak. At this point, the crystalline phase consists of LTSO, LTO and SiO_2 . However, with an increase in the ZrO_2 content, the intensity of the LTSO primary peak gradually strengthens, the LTO diffraction peak disappears and the 26.5° diffraction peak shifts towards the $(\bar{1}12)$ crystal plane diffraction peak of LTSO phase. This indicates a reduction in

the relative SiO_2 content. These changes are a consequence of the introduction of ZrO_2 , which increases the liquid phase volume, thereby altering the overall coordination environment. This alteration inhibits the formation of precipitated phases and enhances the crystallinity of the main phase. Due to LTSE's excellent ionic conductivity, improving its crystalline performance will contribute to enhancing the ionic conductivity of the glass-ceramic electrolyte.

The $\text{Li}_{1+x}\text{Ta}_{1-x}\text{Zr}_x\text{SiO}_5$ glass-ceramic electrolyte samples were examined using scanning electron microscopy (SEM) after 5% HF etching for 10 s. The resulting SEM images are presented in Fig. 6. The images reveal that in the absence of doping ($x = 0$), the shape of the grains is irregular and the grain size is generally large. As the ZrO_2 content increases, the grain size decreases. Despite the presence of some small pores, the

grains are more closely packed together in the form of small particles. When the Zr^{4+} content increases further ($x > 0.1$), the grain continues to grow and the porosity and pore size increase. The HF corrosion of glass-ceramics removes the glass matrix adhering between the grains, showing a surface layer of crystals. The generation of stomata and the increase in pore size indicate a higher proportion of glass in the electrolyte sample. The presence of excess amorphous phase hinders the

conduction of lithium ions, thereby affecting the electrochemical performance of glass-ceramic samples.

Figure 7 illustrates the change of density with Zr^{4+} content in the $Li_{1+x}Ta_{1-x}Zr_xSiO_5$ glass-ceramics. As it can be seen, the density first increases and then decreases, reaching a maximum value of 5.12 g/cm^3 at $x = 0.1$. XRD and SEM analyses reveal that the replacement of Ta^{5+} by Zr^{4+} enhances the crystallinity of $LiTaSiO_5$ in the glass samples and results in grain refinement, leading to improved densification of the glass-ceramics. However, an excess of Zr^{4+} in the system induces the growth of grains and hinders the pre-crystallization process of the precursor glass, which leads to an increase in the amorphous phase content. As a result, the overall density of the glass-ceramics decreases.

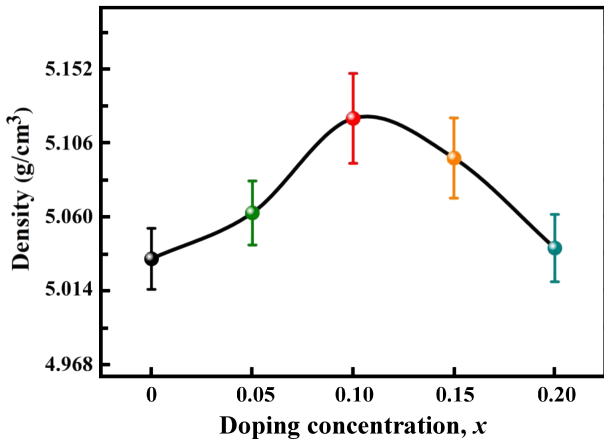


Figure 7. Density of $Li_{1+x}Ta_{1-x}Zr_xSiO_5$ glass-ceramics

3.3. Electrochemical properties

The impedance spectra of the $Li_{1+x}Ta_{1-x}Zr_xSiO_5$ glass and glass-ceramics are shown in Fig. 8a,b. The conductivity values for the glass and glass-ceramic samples are tabulated in Table 3. In Fig. 8a, R_1 denotes the grain impedance, while CPE_1 represents the constant phase element. For the precursor glass samples the conductivity initially increases and then decreases with increasing x . With doping, the large Zr^{4+} ions replace Ta^{5+} in the glass network structure, which increases the lithium ion

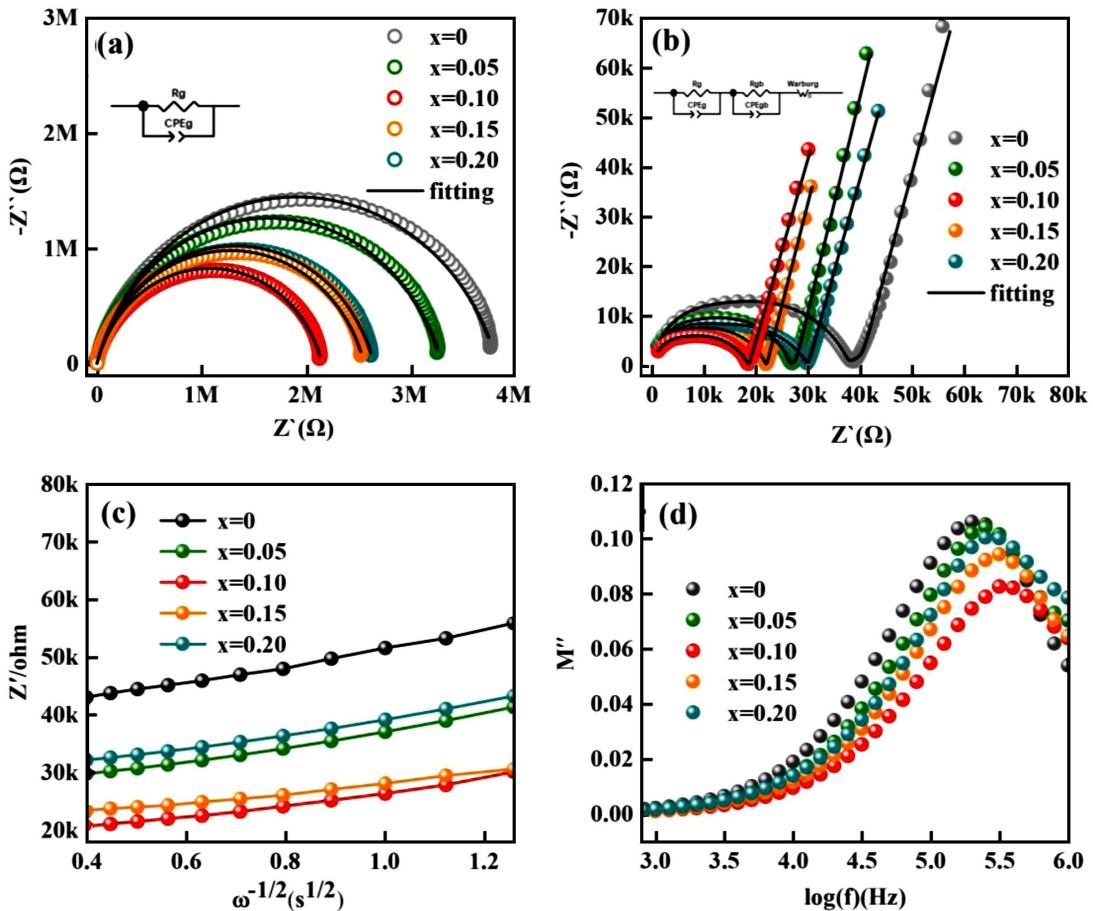


Figure 8. Nyquist plots of precursor glasses (a) and $Li_{1+x}Ta_{1-x}Zr_xSiO_5$ glass-ceramics (b); the relationship between $Z' - \omega^{-1/2}$ (c) and $M'' - f$ (d) of $Li_{1+x}Ta_{1-x}Zr_xSiO_5$ glass-ceramics

Table 3. Ionic conductivity, activation energy and density of $\text{Li}_{1+x}\text{Ta}_{1-x}\text{Zr}_x\text{SiO}_5$ precursor glass and glass-ceramics

Sample	Glass conductivity [S/cm]	Glass-ceramics conductivity [S/cm]	Glass-ceramics density [g/cm ³]	Activation energy [eV]
LiTaSiO_5	5.20×10^{-8}	4.89×10^{-6}	5.03	0.34
$\text{Li}_{1.05}\text{Ta}_{0.95}\text{Zr}_{0.05}\text{SiO}_5$	5.86×10^{-8}	5.94×10^{-6}	5.06	0.33
$\text{Li}_{1.1}\text{Ta}_{0.9}\text{Zr}_{0.1}\text{SiO}_5$	1.00×10^{-7}	8.40×10^{-6}	5.12	0.27
$\text{Li}_{1.15}\text{Ta}_{0.85}\text{Zr}_{0.15}\text{SiO}_5$	7.16×10^{-8}	6.71×10^{-6}	5.09	0.31
$\text{Li}_{1.2}\text{Ta}_{0.8}\text{Zr}_{0.2}\text{SiO}_5$	7.08×10^{-8}	4.55×10^{-6}	5.04	0.30

content, broadens the lithium ion transport channel and facilitates the improvement of lithium ionic conductivity. However, when the number of lithium ions exceeds the limit of the transport channel containment, the ion migration efficiency decreases, resulting in a decrease in the ionic conductivity of the glass [34,35].

Comparing the ionic conductivities of the precursor glass and glass-ceramics samples (Table 3) it can be observed that the trends in conductivity for both materials are similar. The highest conductivity value (8.40×10^{-6} S/cm) was recorded for the glass-ceramic sample with $x = 0.1$. This conductivity value is approximately two orders of magnitude higher than the corresponding value for the precursor glass sample and twice as high as the undoped glass-ceramic sample. The Nyquist plot of the $\text{Li}_{1+x}\text{Ta}_{1-x}\text{Zr}_x\text{SiO}_5$ glass-ceramics revealed that the grain boundary response semicircular arc is larger than the grain response semicircular arc. This indicates that the grain boundary impedance of the sample is larger than that of grain. Upon doping the Zr element into the $\text{Li}_{1+x}\text{Ta}_{1-x}\text{Zr}_x\text{SiO}_5$ sample, the radius of the semicircular arc representing the grain boundary resistance begins to decrease and with $x = 0.10$, the grain boundary semicircular arc radius reaches the minimum. This promotes the formation of conductive LTSO phase due to Zr^{4+} doping and improves the ionic conductivity of glass. In addition, conductive glass fills the pores between the grains, reducing excessive grain boundary resistance in ceramic electrolyte material. This creates a bridge for lithium ions to cross the grain boundaries, transforming the transport mechanism of lithium ions from pure bulk-phase transport to crystalline and amorphous interface transport [36].

Change of the real impedance (Z') with angular frequency ($\omega^{-1/2}$) was also analysed (Fig. 8c) and linear relationship was confirmed. Increased ZrO_2 content in the ceramics initially reduces and then increases the intercept with the Y-axis, indicating changes in Li^+ ion diffusion resistance. Incorporating the appropriate amount of Zr^{4+} into the lattice, by replacing Ta^{5+} and creating an ion vacancy compensated by Li^+ ions, lowers the energy needed for Li^+ ion migration. For the sample with $x = 0.1$, Li^+ ion diffusion resistance is minimized, resulting in maximal ionic conductivity.

Figure 8d illustrates the electric modulus M'' distribution with the logarithm of frequency ($\log f$) for various Zr^{4+} doping levels. The electric modulus provides a more accurate description of the dielectric relaxation

behaviour within the glass-ceramics. The electric modulus relationship was defined as follows:

$$M(\omega) = M' + jM'' = j \cdot \omega \cdot \varepsilon_0 \cdot Z(\omega) \frac{1}{\varepsilon(\omega)} \quad (5)$$

where M' and M'' are the real and imaginary parts of the electric modulus, ε_0 is vacuum permittivity and $\varepsilon(\omega)$ is complex permittivity. Analysis shows the increased Zr^{4+} ion doping shifts the electric modulus peak frequency (f_{max}) to higher frequencies while decreasing the peak intensity. This suggests Zr^{4+} integration into the lattice, reducing the ceramics' dielectric constant. Increased doping initially reduces and then increases the electric modulus peak, corresponding to the peak frequency changes. This indicates that appropriate Zr^{4+} doping reduces the dielectric constant of LTSO, expanding the frequency range for long-range ion migration (from $10^{5.3}$ to $10^{5.5}$). This enhanced ion transport capacity results from widened pathways due to the doping. However, excessive Zr^{4+} doping shifts the electric modulus peak back with increased intensity, leading to higher migration losses.

The Arrhenius plots with fitting lines for the $\text{Li}_{1+x}\text{Ta}_{1-x}\text{Zr}_x\text{SiO}_5$ glass-ceramics in temperature range of 25–150 °C are shown in Fig. 9 and the corresponding activation energies are given in Table 3. As the Zr^{4+} doping content increases, the conductivity activation energy at first decreases and then increases, with the minimum value (for $x = 0.10$) being 0.27 eV. This changing trend of conductivity activation energy suggests that the sub-

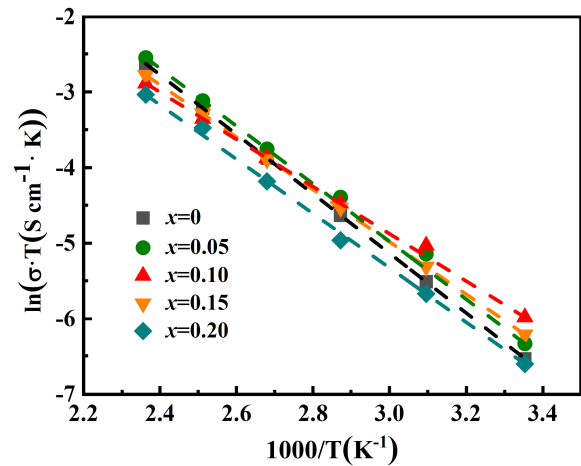
**Figure 9.** Arrhenius diagram of ionic conductivity of $\text{Li}_{1+x}\text{Ta}_{1-x}\text{Zr}_x\text{SiO}_5$ glass-ceramics

Table 4. Comparison of the electrical properties of three different structures of LiTaSiO₅ materials

Composition	Structure	σ_{25} [S/cm]	E_a [eV]	Reference
LiTaSiO ₅	ceramics	5.73×10^{-7}	0.46	[18]
LiTaSiO ₅	ceramics	3.11×10^{-7}	0.70	[16]
LiTaSiO ₅	glass-ceramics	4.89×10^{-6}	0.34	This work

stitution of Zr⁴⁺ for Ta⁵⁺ sites leads to an increase in the lattice constant, expands the lithium-ion transport channels and improves their continuity, ultimately resulting in a decrease in the conductivity activation energy of the samples. The ionic conductivity and activation energy of the LTSO have been compared to previous reports and listed in Table 4. The electrical conductivity of the LTSO glass-ceramic material prepared in this work is nearly one order of magnitude higher than that of the LTSO ceramic materials reported in other studies [16,18]. The glass-ceramics demonstrates a heightened degree of atomic-level disorder when compared to fully crystalline ceramics, thereby facilitating enhanced ionic mobility and promoting accelerated ionic conduction. Moreover, the glass-ceramic material showcases a distinct mode of transport wherein ions migrate at the interface between the crystalline and amorphous phases. This process operates under a low activation energy mechanism [37], leading to a significantly low activation energy of 0.34 eV for LTSO.

IV. Conclusions

Different Li₂O-Ta₂O₅-SiO₂ glasses in which Ta₂O₅ was partially substituted by ZrO₂ were prepared by melt quenching method. It was shown that appropriate amount of ZrO₂ plays the role of intermediate in the glass mesh, increases the content of non-bridging oxygen, enhances the tightness of the structural connection and makes the glass denser. At the same time, the transition temperature and crystallization temperature of the glass are lowered because ZrO₂ partially replaces Ta₂O₅. However, with the further increase of the doping content, the network structure of the glass becomes too dense and the migration of lithium ions under the electric field is hindered, so that the ionic conductivity of the glass decreases. The precursor glass was heat treated at 980 °C for 10 h to obtain Li_{1+x}Ta_{1-x}Zr_xSiO₅ (x = 0, 0.05, 0.1, 0.15 and 0.2) glass-ceramics. The results showed that Zr⁴⁺ doping inhibited the precipitation of dielectric phase LiTaO₃. In addition, Zr⁴⁺ doping also improved the room temperature ionic conductivity of this glass-ceramic system, which reached 8.40×10^{-6} S/cm when x = 0.1, nearly 2 times higher than that of the undoped Zr⁴⁺ glass-ceramics, and the activation energy was reduced to 0.27 eV.

Acknowledgements: This work was supported by “Key Project of Science and Technology of Jiangxi Provincial Department of Education (GJJ2200804, GJJ200844)”, “Double Thousand” Program project of Jiangxi Province and the high-level talents research

start-up project of Jiangxi University of Science and Technology.

References

1. J. He, J. Meng, Y. Huang, “Challenges and recent progress in fast-charging lithium-ion battery materials”, *J. Power Sources*, **570** (2023) 232965.
2. J.G. Kim, B. Son, S. Mukherjee, N. Schuppert, A. Bates, O. Kwon, M.J. Choi, H.Y. Chung, S. Park, “A review of lithium and non-lithium based solid state batteries”, *J. Power Sources*, **282** (2015) 299–322.
3. Q. Xia, S. Sun, J. Xu, F. Zan, J. Yue, Q. Zhang, L. Gu, H. Xia, “Self-standing 3D cathodes for all-solid-state thin film lithium batteries with improved interface kinetics”, *Small*, **14** [52] (2018) e1804149.
4. F. Zheng, M. Kotobuki, S. Song, M.O. Lai, L. Lu, “Review on solid electrolytes for all-solid-state lithium-ion batteries”, *J. Power Sources*, **389** (2018) 198–213.
5. D. Wang, G. Zhong, O. Dolotko, Y. Li, M.J. McDonald, J. Mi, R. Fu, Y. Yang, “The synergistic effects of Al and Te on the structure and Li⁺-mobility of garnet-type solid electrolytes”, *J. Mater. Chem. A*, **2** [47] (2014) 20271–20279.
6. N. Kamaya, K. Homma, Y. Yamakawa, M. Hirayama, R. Kanno, M. Yonemura, T. Kamiyama, Y. Kato, S. Hama, K. Kawamoto, A. Mitsui, “A lithium superionic conductor”, *Nat. Mater.*, **10** [9] (2011) 682–686.
7. Y. Seino, T. Ota, K. Takada, A. Hayashi, M. Tatsumisago, “A sulphide lithium super ion conductor is superior to liquid ion conductors for use in rechargeable batteries”, *Energy Environ. Sci.*, **7** [2] (2014) 627–631.
8. V. Thangadurai, S. Narayanan, D. Pinzaru, “Garnet-type solid-state fast Li ion conductors for Li batteries: Critical review”, *Chem. Soc. Rev.*, **43** [13] (2014) 4714–4727.
9. R. Murugan, V. Thangadurai, W. Weppner, “Fast lithium ion conduction in garnet-type Li₇La₃Zr₂O₁₂”, *Angew. Chem., Int. Ed. Engl.*, **46** [41] (2007) 7778–7781.
10. Y-T. Wang, X. Chen, “Single crystal growth and electrochemical studies of garnet-type fast Li-ion conductors”, *Tungsten*, **4** [4] (2022) 263–268.
11. Y-J. Liu, R-Y. Fang, D. Mitlin, “NASICON solid electrolyte coated by indium film for all-solid-state Li-metal batteries”, *Tungsten*, **4** [4] (2022) 316–322.
12. H. Aono, E. Sugimoto, Y. Sadaoka, N. Imanaka, G.-Y. Adachi, “Electrical properties of sintered lithium titanium phosphate ceramics (Li_{1+x}M_xTi_{2-x}(PO₄)₃, M³⁺ = Al³⁺, Sc³⁺, or Y³⁺)”, *Chem. Lett.*, **19** [10] (1990) 1825–1828.
13. L. Tan, J.C. Mauro, J. Peng, X. Yang, M. Peng, “Quantitative prediction of the structure and properties of Li₂O-Ta₂O₅-SiO₂ glasses via phase diagram approach”, *J. Am. Ceram. Soc.*, **102** [1] (2019) 185–194.
14. J.F. Ortiz-Mosquera, A.M. Nieto-Muñoz, A.C.M. Rodrigues, “Precursor glass stability, microstructure and ionic conductivity of glass-ceramics from the Na_{1+x}Al_xGe_{2-x}(PO₄)₃ NASICON series”, *J. Non-Cryst. Solids*, **513** (2019) 36–43.

15. A. Ibrahim, K. Kubo, S. Watanabe, S. Shiba, I. Khan, B. Zhang, Z. Homonnay, E. Kuzmann, L. Pavić, A. Sanić, “Enhancement of electrical conductivity and thermal stability of iron-or tin-substituted vanadate glass and glass-ceramics nanocomposite to be applied as a high-performance cathode active material in sodium-ion batteries”, *J. Alloys Compd.*, **930** (2023) 167366.
16. S. Xiong, X. He, A. Han, Z. Liu, Z. Ren, B. McElhenny, A.M. Nolan, S. Chen, Y. Mo, H. Chen, “Computation-guided design of LiTaSiO₅, a new lithium ionic conductor with sphene structure”, *Adv. Energy Mater.*, **9** [22] (2019) 1803821.
17. Y. Zhang, S. Liu, Q. Zhang, T. Ning, X. Wang, A. Lu, “Effect of Nb⁵⁺ doping on the microstructure and conductivity of Li_{1.125}Ta_{0.875}Zr_{0.125}SiO₅ electrolyte”, *J. Alloys Compd.*, **902** (2022) 163760.
18. Q. Wang, J.F. Wu, Z. Lu, F. Ciucci, W.K. Pang, X. Guo, “A new lithium-ion conductor LiTaSiO₅: Theoretical prediction, materials synthesis, and ionic conductivity”, *Adv. Funct. Mater.*, **29** [37] (2019) 1904232.
19. W. Ślubowska, K. Kwatek, C. Jastrzębski, J.L. Nowiński, “Thermal, structural and electrical study of boron-incorporated LATP glasses and glass-ceramics”, *Solid State Ionics*, **335** (2019) 129–134.
20. S. Pershina, B. Antonov, A. Farlenkov, E. Vovkotrub, “Glass-ceramics in Li_{1+x}Al_xGe_{2-x}(PO₄)₃ system: the effect of Al₂O₃ addition on microstructure, structure and electrical properties”, *J. Alloys Compd.*, **835** (2020) 155281.
21. M. Sitarz, “The structure of simple silicate glasses in the light of middle infrared spectroscopy studies”, *J. Non-Cryst. Solids*, **357** [6] (2011) 1603-1608.
22. C. Jiang, D. Ramteke, J. Li, R. Sliz, H. Sreenivasan, C. Cheeseman, P. Kinnunen, “Preparation and characterization of binary Mg-silicate glasses via sol-gel route”, *J. Non-Cryst. Solids*, **606** (2023) 122204.
23. R.V. Goncalves, R. Wojcieszak, P.M. Uberman, S.R. Teixeira, L.M. Rossi, “Insights into the active surface species formed on Ta₂O₅ nanotubes in the catalytic oxidation of CO”, *Phys. Chem. Chem. Phys.*, **16** [12] (2014) 5755–5762.
24. N.A. El-Shafi, M. Morsi, “Optical absorption and infrared studies of some silicate glasses containing titanium”, *J. Mater. Sci.*, **32** (1997) 5185–5189.
25. L. Cordeiro, R.M. Silva, G.M. de Pietro, C. Pereira, E.A. Ferreira, S.J. Ribeiro, Y. Messaddeq, F.C. Cassanjes, G. Poirier, “Thermal and structural properties of tantalum alkali-phosphate glasses”, *J. Non-Cryst. Solids*, **402** (2014) 44–48.
26. S. Al-Ani, C. Hogarth, R. El-Malawany, “A study of optical absorption in tellurite and tungsten-tellurite glasses”, *J. Mater. Sci.*, **20** (1985) 661–667.
27. K. Ariane, A. Tamayo, A. Chorfa, F. Rubio, J. Rubio, “Effect of P₂O₅ and Al₂O₃ on crystallization, structure, microstructure and properties of Li₂O-MgO-Al₂O₃-SiO₂-TiO₂-ZrO₂ glass ceramics”, *Bol. Soc. Esp. Ceram. Vidrio*, **61** [2] (2022) 146–159.
28. S.-W. Lee, R.A. Condrate, “The infrared and Raman spectra of ZrO₂-SiO₂ glasses prepared by a sol-gel process”, *J. Mater. Sci.*, **23** (1988) 2951–2959.
29. D.A. McKeown, I.S. Muller, A.C. Buechele, I.L. Pegg, C.A. Kendziora, “Structural characterization of high-zirconia borosilicate glasses using Raman spectroscopy”, *J. Non-Cryst. Solids*, **262** [1-3] (2000) 126–134.
30. C.M. Muiva, S.T. Sathiaraj, J.M. Mwabora, “Crystallisation kinetics, glass forming ability and thermal stability in glassy Se_{100-x}In_x chalcogenide alloys”, *J. Non-Cryst. Solids*, **357** [22-23] (2011) 3726–3733.
31. K. Öksüz, Ş. Şen, U. Şen, “Influence of ZrO₂ addition on the structure and dielectric properties of BaTiO₃ ceramics”, *Acta Phys. Pol. A*, **131** [1] (2017) 197–199.
32. K. Öksüz, Ş. Şen, U. Şen, “Effects of B₂O₃ Addition on the sintering behavior of 0-5-10% ZrO₂ doped BaTiO₃ based ceramics”, *Acta Phys. Pol. A*, **127** [4] (2015) 1086–1089.
33. K. Öksüz, Ş. Şen, U. Şen, “Microstructural evaluation and characterization of solid-state reaction of B₂O₃ doped BaZr_xTi_{1-x}O₃ ceramics”, *J. Aust. Ceram.*, **51** [2] (2015) 137–143.
34. S. Banijamali, T. Ebadzadeh, “Glass-forming ability, sinter-crystallization behavior and microwave dielectric properties of MgO-B₂O₃-(Al₂O₃)-SiO₂ glass-ceramics”, *J. Non-Cryst. Solids*, **441** (2016) 34–41.
35. R.R. Gonçalves, Y. Messaddeq, A. Chiasera, Y. Jestin, M. Ferrari, S.J. Ribeiro, “Erbium-activated silica-zirconia planar waveguides prepared by sol-gel route”, *Thin Solid Films*, **516** [10] (2008) 3094–3097.
36. R. Murugan, V. Thangadurai, W. Weppner, “Lithium ion conductivity of Li_{5+x}Ba_xLa_{3-x}Ta₂O₁₂ (x = 0–2) with garnet-related structure in dependence of the barium content”, *Ionics*, **13** [4] (2007) 195–203.
37. A. Schirmeisen, A. Taskiran, H. Fuchs, H. Bracht, S. Murugavel, B. Roling, “Fast interfacial ionic conduction in nanostructured glass ceramics”, *Phys. Rev. Lett.*, **98** [22] (2007) 225901.